Towards two-photon excited endogenous fluorescence lifetime imaging microendoscopy

C.H. Hage, P. Leclerc, J. Brevier, M. Fabert, C. Le Nézet, A. Kudlinski, L. Héliot, D F. Louradour

Research Article | Vol. 9, No. 1 | 1 Jan 2018 | BIOMEDICAL OPTICS EXPRESS 142
Biomedical Optics EXPRESS

Towards two-photon excited endogenous fluorescence lifetime imaging microendoscopy

C. H. HAGE,[1,*] P. LECLERC,[1] J. BREVIER,[1] M. FABERT,[1] C. LE NÉZET,[2] A. KUDLINSKI,[2] L. HÉLIOT,[2] AND F. LOURADOUR[1]

[1]*Université de Limoges, XLIM, UMR CNRS 7252, 123 Avenue A. Thomas, 87060 Limoges, France*
[2]*Univ. Lille, CNRS, UMR 8523 – PhLAM – Physique des Lasers, Atomes et Molécules, F-59000 Lille, France*
[*]*charles-henri.hage@unilim.fr*

Abstract: *In situ* fluorescence lifetime imaging microscopy (FLIM) in an endoscopic configuration of the endogenous biomarker nicotinamide adenine dinucleotide (NADH) has a great potential for malignant tissue diagnosis. Moreover, two-photon nonlinear excitation provides intrinsic optical sectioning along with enhanced imaging depth. We demonstrate, for the first time to our knowledge, nonlinear endogenous FLIM in a fibered microscope with proximal detection, applied to NADH in cultured cells, as a first step to a nonlinear endomicroscope, using a double-clad microstructured fiber with convenient fiber length (> 3 m) and excitation pulse duration (≈50 fs). Fluorescence photons are collected by the fiber inner cladding and we show that its contribution to the impulse response function (IRF), which originates from its intermodal and chromatic dispersions, is small (< 600 ps) and stable for lengths up to 8 m and allows for short lifetime measurements. We use the phasor representation as a quick visualization tool adapted to the endoscopy speed requirements.

OCIS codes: (060.2310) Fiber optics; (170.2150) Endoscopic imaging; (170.2520) Fluorescence microscopy; (170.6920) Time-resolved imaging; (180.4315) Nonlinear microscopy; (170.3880) Medical and biological imaging.

References and links

1. J. T. C. Liu, N. O. Loewke, M. J. Mandella, R. M. Levenson, J. M. Crawford, and C. H. Contag, "Point-of-care pathology with miniature microscopes," Anal. Cell Pathol. (Amst.) **34**(3), 81–98 (2011).
2. J. Condeelis and J. E. Segall, "Intravital imaging of cell movement in tumours," Nat. Rev. Cancer **3**(12), 921–930 (2003).
3. K. O. Alfarouk, D. Verduzco, C. Rauch, A. K. Muddathir, A. H. Bashir, G. O. Elhassan, M. E. Ibrahim, J. D. Orozco, R. A. Cardone, S. J. Reshkin, and S. Harguindey, "Glycolysis, tumor metabolism, cancer growth and dissemination. A new pH-based etiopathogenic perspective and therapeutic approach to an old cancer question," Oncoscience **2**(4), 317 (2014).
4. J. R. Lakowicz, H. Szmacinski, K. Nowaczyk, and M. L. Johnson, "Fluorescence lifetime imaging of free and protein-bound NADH," Proc. Natl. Acad. Sci. U.S.A. **89**(4), 1271–1275 (1992).
5. C. Stringari, A. Cinquin, O. Cinquin, M. A. Digman, P. J. Donovan, and E. Gratton, "Phasor approach to fluorescence lifetime microscopy distinguishes different metabolic states of germ cells in a live tissue," Proc. Natl. Acad. Sci. U.S.A. **108**(33), 13582–13587 (2011).
6. Q. Yu and A. A. Heikal, "Two-photon autofluorescence dynamics imaging reveals sensitivity of intracellular NADH concentration and conformation to cell physiology at the single-cell level," J. Photochem. Photobiol. B **95**(1), 46–57 (2009).
7. M. C. Skala, K. M. Riching, D. K. Bird, A. Gendron-Fitzpatrick, J. Eickhoff, K. W. Eliceiri, P. J. Keely, and N. Ramanujam, "In vivo multiphoton fluorescence lifetime imaging of protein-bound and free nicotinamide adenine dinucleotide in normal and precancerous epithelia," J. Biomed. Opt. **12**(2), 024014 (2007).
8. M. C. Skala, K. M. Riching, A. Gendron-Fitzpatrick, J. Eickhoff, K. W. Eliceiri, J. G. White, and N. Ramanujam, "In vivo multiphoton microscopy of {NADH} and {FAD} redox states, fluorescence lifetimes, and cellular morphology in precancerous epithelia," Proc. Natl. Acad. Sci. U.S.A. **104**(49), 19494–19499 (2007).
9. Y. Sun, J. E. Phipps, J. Meier, N. Hatami, B. Poirier, D. S. Elson, D. G. Farwell, and L. Marcu, "Endoscopic fluorescence lifetime imaging for in vivo intraoperative diagnosis of oral carcinoma," Microsc. Microanal. **19**(4), 791–798 (2013).

#307290 https://doi.org/10.1364/BOE.9.000142
Journal © 2018 Received 18 Sep 2017; revised 16 Nov 2017; accepted 4 Dec 2017; published 8 Dec 2017

Biomedical Optics EXPRESS

10. C. Stringari, J. L. Nourse, L. A. Flanagan, and E. Gratton, "Phasor Fluorescence Lifetime Microscopy of Free and Protein-Bound NADH Reveals Neural Stem Cell Differentiation Potential," PLoS One **7**(11), e48014 (2012).
11. R. Datta, C. Heylman, S. C. George, and E. Gratton, "Label-free imaging of metabolism and oxidative stress in human induced pluripotent stem cell-derived cardiomyocytes," Biomed. Opt. Express **7**(5), 1690–1701 (2016).
12. R. Datta, A. Alfonso-García, R. Cinco, and E. Gratton, "Fluorescence lifetime imaging of endogenous biomarker of oxidative stress," Sci. Rep. **5**(1), 9848 (2015).
13. C. Xu, W. Zipfel, J. B. Shear, R. M. Williams, and W. W. Webb, "Multiphoton fluorescence excitation: new spectral windows for biological nonlinear microscopy," Proc. Natl. Acad. Sci. U.S.A. **93**(20), 10763–10768 (1996).
14. P. G. Bush, D. L. Wokosin, and A. C. Hall, "Two-versus one photon excitation laser scanning microscopy: critical importance of excitation wavelength," Front. Biosci. **12**(1), 2646–2657 (2007).
15. J. M. Squirrell, D. L. Wokosin, J. G. White, and B. D. Bavister, "Long-term two-photon fluorescence imaging of mammalian embryos without compromising viability," Nat. Biotechnol. **17**(8), 763–767 (1999).
16. D. K. Bird, L. Yan, K. M. Vrotsos, K. W. Eliceiri, E. M. Vaughan, P. J. Keely, J. G. White, and N. Ramanujam, "Metabolic mapping of MCF10A human breast cells via multiphoton fluorescence lifetime imaging of the coenzyme NADH," Cancer Res. **65**(19), 8766–8773 (2005).
17. K. König, A. Uchugonova, and E. Gorjup, "Multiphoton fluorescence lifetime imaging of 3D-stem cell spheroids during differentiation," Microsc. Res. Tech. **74**(1), 9–17 (2011).
18. C. S. Garbe, A. Buttgereit, S. Schürmann, and O. Friedrich, "Automated multiscale morphometry of muscle disease from second harmonic generation microscopy using tensor-based image processing," IEEE Trans. Biomed. Eng. **59**(1), 39–44 (2012).
19. W. Göbel, J. N. D. Kerr, A. Nimmerjahn, and F. Helmchen, "Miniaturized two-photon microscope based on a flexible coherent fiber bundle and a gradient-index lens objective," Opt. Lett. **29**(21), 2521–2523 (2004).
20. C. M. Brown, D. R. Rivera, I. Pavlova, D. G. Ouzounov, W. O. Williams, S. Mohanan, W. W. Webb, and C. Xu, "In vivo imaging of unstained tissues using a compact and flexible multiphoton microendoscope," J. Biomed. Opt. **17**(4), 040505 (2012).
21. G. Ducourthial, P. Leclerc, T. Mansuryan, M. Fabert, J. Brevier, R. Habert, F. Braud, R. Batrin, C. Vever-Bizet, G. Bourg-Heckly, L. Thiberville, A. Druilhe, A. Kudlinski, and F. Louradour, "Development of a real-time flexible multiphoton microendoscope for label-free imaging in a live animal," Sci. Rep. **5**(1), 18303 (2016).
22. H. Sparks, S. Warren, J. Guedes, N. Yoshida, T. C. Charn, N. Guerra, T. Tatla, C. Dunsby, and P. French, "A flexible wide-field FLIM endoscope utilising blue excitation light for label-free contrast of tissue," J. Biophotonics **8**(1-2), 168–178 (2015).
23. G. T. Kennedy, H. B. Manning, D. S. Elson, M. A. A. Neil, G. W. Stamp, B. Viellerobe, F. Lacombe, C. Dunsby, and P. M. W. French, "A fluorescence lifetime imaging scanning confocal endomicroscope," J. Biophotonics **3**(1-2), 103–107 (2010).
24. S. Cheng, J. J. Rico-Jimenez, J. Jabbour, B. Malik, K. C. Maitland, J. Wright, Y.-S. L. Cheng, and J. A. Jo, "Flexible endoscope for continuous in vivo multispectral fluorescence lifetime imaging," Opt. Lett. **38**(9), 1515–1517 (2013).
25. G. O. Fruhwirth, S. Ameer-Beg, R. Cook, T. Watson, T. Ng, and F. Festy, "Fluorescence lifetime endoscopy using TCSPC for the measurement of FRET in live cells," Opt. Express **18**(11), 11148–11158 (2010).
26. F. Knorr, D. R. Yankelevich, J. Liu, S. Wachsmann-Hogiu, and L. Marcu, "Two-photon excited fluorescence lifetime measurements through a double-clad photonic crystal fiber for tissue micro-endoscopy," J. Biophotonics **5**(1), 14–19 (2012).
27. W. Liang, G. Meng, I. Gannot, M.-J. Li, and X. Li, "Real-time Fluorescence Lifetime Imaging by a Fiber-optic Two-photon Endomicroscopy System," in *Biomedical Optics 2016*, OSA Technical Digest (Online) (Optical Society of America, 2016), p. TTu4B.3.
28. M. Weinigel, H. G. Breunig, P. Fischer, M. Kellner-Höfer, R. Bückle, and K. König, "Clinical multiphoton endoscopy with FLIM capability," in (2013), Vol. 8588, p. 85882E–8588–9.
29. M. Kalashyan, C. Lefort, L. Martínez-León, T. Mansuryan, L. Mouradian, and F. Louradour, "Ultrashort pulse fiber delivery with optimized dispersion control by reflection grisms at 800 nm," Opt. Express **20**(23), 25624–25635 (2012).
30. S. Huang, A. A. Heikal, and W. W. Webb, "Two-photon fluorescence spectroscopy and microscopy of NAD(P)H and flavoprotein," Biophys. J. **82**(5), 2811–2825 (2002).
31. J. N. Kutz, J. A. Cox, and D. Smith, "Mode mixing and power diffusion in multimode optical fibers," J. Lightwave Technol. **16**(7), 1195–1202 (1998).
32. J. Carpenter, B. J. Eggleton, and J. Schröder, "110x110 optical mode transfer matrix inversion," Opt. Express **22**(1), 96–101 (2014).
33. W. Xiong, P. Ambichl, Y. Bromberg, B. Redding, S. Rotter, and H. Cao, "Principal modes in multimode fibers: exploring the crossover from weak to strong mode coupling," Opt. Express **25**(3), 2709–2724 (2017).
34. C. H. Hage, B. Kibler, E. R. Andresen, S. Michel, H. Rigneault, A. Courjaud, E. Mottay, J. M. Dudley, G. Millot, and C. Finot, "Optimization and characterization of a femtosecond tunable light source based on the soliton self-frequency shift in photonic crystal fiber," Proc. SPIE **8071**, 80710I (2011).
35. M. A. Digman, V. R. Caiolfa, M. Zamai, and E. Gratton, "The phasor approach to fluorescence lifetime imaging analysis," Biophys. J. **94**(2), L14–L16 (2008).

Biomedical Optics EXPRESS

36. J. M. Dudley and S. Coen, "Supercontinuum generation in photonic crystal fiber," Rev. Mod. Phys. **78**(4), 1135–1184 (2006).
37. A. Leray, S. Padilla-Parra, J. Roul, L. Héliot, and M. Tramier, "827Spatio-Temporal Quantification of FRET in Living Cells by Fast Time-Domain FLIM: A Comparative Study of Non-Fitting Methods," PLoS One **8**, e69335 (2013).
38. D. A. Peyrot, C. Lefort, M. Steffenhagen, T. Mansuryan, G. Ducourthial, D. Abi-Haidar, N. Sandeau, C. Vever-Bizet, S. G. Kruglik, L. Thiberville, F. Louradour, and G. Bourg-Heckly, "Development of a nonlinear fiber-optic spectrometer for human lung tissue exploration," Biomed. Opt. Express **3**(5), 840–853 (2012).
39. I. H. Malitson, "Interspecimen Comparison of the Refractive Index of Fused Silica," J. Opt. Soc. Am. **55**(10), 1205 (1965).
40. W. Becker, "The bh TCSPC Handbook," Scanning **2015**, 1–768 (2015).
41. S. Jerebtsov, A. Kolomenskii, M. Poudel, F. Zhu, and H. Schuessler, "Lifetime and anisotropy decay of excited Coumarin 30 measured by a femtosecond pump–probe technique," J. Mod. Opt. **53**(16-17), 2609–2617 (2006).
42. I. Georgakoudi, B. C. Jacobson, M. G. Müller, E. E. Sheets, K. Badizadegan, D. L. Carr-Locke, C. P. Crum, C. W. Boone, R. R. Dasari, J. Van Dam, and M. S. Feld, "NAD(P)H and collagen as in vivo quantitative fluorescent biomarkers of epithelial precancerous changes," Cancer Res. **62**(3), 682–687 (2002).
43. A. V. Kuznetsov, O. Mayboroda, D. Kunz, K. Winkler, W. Schubert, and W. S. Kunz, "Functional imaging of mitochondria in saponin-permeabilized mice muscle fibers," J. Cell Biol. **140**(5), 1091–1099 (1998).
44. K. Jung, P. Kim, F. Leuschner, R. Gorbatov, J. K. Kim, T. Ueno, M. Nahrendorf, and S. H. Yun, "Endoscopic time-lapse imaging of immune cells in infarcted mouse hearts," Circ. Res. **112**(6), 891–899 (2013).
45. J. L. Rinnenthal, C. Börnchen, H. Radbruch, V. Andresen, A. Mossakowski, V. Siffrin, T. Seelemann, H. Spiecker, I. Moll, J. Herz, A. E. Hauser, F. Zipp, M. J. Behne, and R. Niesner, "Parallelized TCSPC for Dynamic Intravital Fluorescence Lifetime Imaging: Quantifying Neuronal Dysfunction in Neuroinflammation," PLoS One **8**(4), e60100 (2013).

1. Introduction

Malignant tissue diagnosis would greatly benefit from a flexible *in vivo in situ* label-free and minimally invasive high resolution imaging tool, capable of several hundreds of microns imaging depth to address a typical epithelium [1]. Especially, tumor genesis and development is associated with cellular migration [2] and impaired cellular metabolism, with a shift from the oxidative phosphorylation to aerobic glycolysis [3], known as the Warburg effect. The Nicotinamide Adenine Dinucleotide (NADH) coenzyme is the principal electron donor in oxidative phosphorylation and electron acceptor in glycolysis. An impaired cellular metabolism induces a change in its enzyme-binding activity and thus a change of its fluorescence properties such as intensity and time exponential decay, called lifetime. Especially, NADH have a free lifetime component of ≈0.4 ns and an enzyme-sensitive bound one of 2.8 to 3.4 ns [4–6]. The higher rate of glycolysis induces a higher free/enzyme-bound ratio and a variation of key-enzyme activity typically associated with a decrease of the long-lifetime component, leading to a faster fluorescence decay. Assessing this faster decay has enabled to discriminate between normal and tumor tissues [7–9] and cells [6]. Study of the NADH lifetime variations is also sensitive enough to be applied to stem cell differentiation [10], cardiac diseases [11] or oxidative stress [12] studies. Fluorescence lifetime has the advantage, over intensity, of its immunity to concentration and quantum yield variations which makes lifetime imaging particularly adapted to *in vivo in situ* imaging.

NADH fluorescence is usually detected around 450 nm and can be linearly excited around 350 nm. However excitation at this wavelength can be phototoxic, suffers from a limited penetration depth and requires a confocal detection scheme to access a spatial resolution in depth. On the other side two-photon excited fluorescence (2PEF) at ≈700-760 nm [13] allows in the same time intrinsic femtoliter spatial resolution with a good spatial sectioning capability, epithelium imaging [8] and reduced phototoxicity due to the increased excitation localization and wavelength [14,15]. Moreover nonlinear FLIM of NADH has been largely demonstrated [8,11,16,17] and the involved excitation source like femtosecond oscillators would also give access to complementary structural or metabolic information like Second Harmonic Generation (SHG) [18] or intensity redox ratio [8].

Previous key works on multiphoton flexible endoscopy do exist [19,20]. We previously demonstrated a nonlinear endomicroscope using a microstructured double-clad silica made (thus fluorescence free) fiber, with a practical fiber length (5-m long), short (sub-40-fs) and

Biomedical Optics EXPRESS

powerful (> 30 mW) excitation pulses @ 810 nm [21]. Recently, we extended our configuration to ≈100-mW and 60-fs @ 760 nm pulses convenient to NADH excitation. Numerous demonstrations of FLIM using linear excitation in an endoscopic configuration, i.e. through a fiber with a proximal detection, exist [9,22–25]. Very few using nonlinear excitation [26,27] and none on endogenous nonlinear imaging, furthermore using a practical fiber length (> 3m). An efficient configuration using a free-space articulated arm has been previously proposed by K. König [28], but its limited flexibility and its bulkiness represent detrimental issues for minimally invasive imaging deeply in the organism, for patients of reduced mobility and, for research ends, for freely moving animal monitoring. The absence of a relevant fibered demonstration occurs because a convenient fiber length raises two issues: the delivery of the ultrashort pulses required for such low two-photon cross-section fluorophores, and the possible influence of the fiber fluorescence collection on the measured lifetimes.

Here we demonstrate, for the first time to our knowledge, that such an imaging modality is possible with a readily usable flexible "handheld fiber microscope" as a first step to endomicroscopy, while our device shows a great potential for dermatology. The optimization of the excitation pulses required a new design of the inner core (see Fig. 1(b)) chromatic dispersion management and is a multi-parameter problem depending on the dispersion management, the fiber injected power and the considered pulse spectrum [29]. This subject is beyond the fibered FLIM measurement issues and will be treated separately, along with other imaging modalities, in a future communication. Regarding the lifetime measurement question, fluorescence photons are collected by a 188-µm in diameter highly multimodal silica second core, which makes the measured lifetimes potentially modified by the intermodal and chromatic dispersions of the waveguide. This situation raises two important questions:

- What is the influence of these dispersions on the system IRF, knowing that fused silica chromatic dispersion is relatively large in the spectral region of interest (≈[430-490] nm) [30] and knowing that the wide collection cladding allows for thousands of modes of visible light to be guided ?

- What is the variability of the IRF during handling the fiber (e.g. by the practitioner during future clinical application), especially of its peak, due to modal condition variations (i.e. bending-induced couplings and filterings) occurring while moving the endoscopic fiber? Although the modal population will remain fairly stable [31–33], this latter questioning is all the more important as NADH lifetime analysis which is the main goal of our work relies on quite subtle changes making the IRF stability a pivotal question.

Surprisingly we only found one study which addresses these questions [22]. So the aim of this paper is to bring an additional insight to this IRF question by applying it to the most used nonlinear microendoscopy configuration (i.e. distal scanning using a monomode excitation/multimode collection double clad fiber). Femtosecond laser setups typically exhibit pulse durations and period variabilities of ≈100 fs [34]. They are not likely to influence the system IRF, so we investigate the fiber influence on the Impulse Response Function (IRF) of our system, using femtosecond and picosecond test signals, for available fiber lengths and collection cladding numerical apertures (NA). Using tools like average lifetime calculation, phasor representation [35] and deconvolution we compare fluorescence lifetime histograms acquired in free space and through our fibers and show their ability to allow for accurate lifetime measurements, even for long (> 5m) fibers. The phasor representation shows a clear separation between short (< 600 ps) and long (> 1.5 ns) lifetimes and highlight the potential of our configuration to distinguish lifetime structures originating from specific metabolism states [6]. Finally we apply our observations in a fiber microscope configuration with proximal detection on NADH-FLIM imaging of HT29 colorectal cancer cells. We make use

Biomedical Optics EXPRESS

of the phasor representation as a fitting-free, and thus straightforward and quick visualization way, compatible with the speed requirements of endoscopy.

2. Materials and methods

2.1 Fiber characterization setup

As the Fig. 1(a) shows, during the imaging (see sect. 2.4), the biological sample excitation is made by injecting a femtosecond laser into the fiber inner core (see the Fig. 1(b) for the fiber geometry description) at the proximal end. The fluorescence is collected by the distal whole inner surface (i.e. {inner core + second core (called "inner cladding in the abstract)}), and travels from this distal end to the proximal one and towards the detector. We studied the influence of the fiber on the measured lifetimes using various laser test signals, simulating the sample fluorescence, injected over this whole distal inner surface. The setup used to characterize the fibers is depicted in Fig. 1(c). The primary source was a Ti:Sa laser (MIRA-900, Coherent, Santa Clara, Ca, USA) pumped by a 15W Verdi laser and producing ≈ 100 fs pulses at 860 nm.

For the study of the intermodal dispersion alone we used two different kinds of relatively narrow bandwidth signal being either:

- direct 860 nm Ti:Sa laser pulses,
- wavelength tunable ultrashort pulses called solitons, generated in a first 35-cm photonic crystal fiber (PCF, called PCF1) which produced, depending on the injection conditions, ≈100 fs / 20 nm-wide pulses with a carrier wavelength ranging from 900 to 1050 nm, through the soliton self-frequency shift (SSFS) process [34] (Fig. 1(d), the SSFS pulse being the one centered on 920 nm). The 860-nm pump residue is subsequently filtered (900 nm long-pass filter ("LPF"), Thorlabs)

On the other side, the combined effects of both chromatic and intermodal dispersions were studied using a short (<2ps) and wide bandwidth supercontinuum (SC) [36], generated in the same fiber PCF1 but using different injection conditions, giving a spectrum spanning from 860 to 1050 nm (figure (d)).

Before being launched to the distal end of the fiber Under Test (FUT), these different infrared test signals (direct Ti:Sa laser, SSFS pulses, SCs) were focused in a BBO crystal to match, by Second Harmonic Generation (SHG), the NADH fluorescence detection range (≈[430:490] nm). Their properties were measured using a fiber-based spectrometer (Thorlabs, CSS175) and an intensity autocorrelator (PulseCheck, APE GmbH, Berlin, Germany).

Additionally to these large bandwidth visible signals, fluorescence lifetime measurements on coumarin 515 (Exciton, Oakley, OH, USA, diluted in ethanol) were performed by focusing directly the primary Ti:Sa laser source into a 1-cm silica spectrometer cuvette (see Fig. 1(c)).

The generated second harmonic/fluorescence signal was isolated from the laser residue (Thorlabs FGB18 and Semrock 720/SP filters) and injected into the FUT with a microscope objective. The numerical aperture (NA, 0.4) of the latter was higher than the FUT collection cladding (0.2 to 0.24) and was used along with a thin film polymer diffuser to populate all the fiber modes. At the fiber proximal output a high collimation objective NA (0.65) avoided eventual fiber mode filtering. This configuration ensures also that any significant mode leaking and mode coupling, e.g. resulting from a strong bending, can be detected. We checked the proper fiber injection using a CCD camera (DCC1545M-GL, Thorlabs). Depending on the wavelength of the signal, filter combinations were added to a 720 nm short-pass one (Semrock 720/SP). The signal was finally detected with a fast photomultiplier tube (PMT) (H7422P-40, Hamamatsu, Japan), amplified (200 MHz bandwidth amplifier, HCA-200M-20K-C, FEMTO Messtechnik GmbH, Berlin, Germany), shaped into 6.5 ns TTL pulses by a discriminator (TDC2000 discriminator, FAST ComTec GmbH, Berlin, Germany) and treated by a 4-ps resolution TCSPC device (PicoHARP, Picoquant GmbH, Jena, Germany)

Biomedical Optics EXPRESS

for lifetime measurements. The time reference was taken from the trigger output of the laser and shaped with a similar discriminator. A flip-flop mirror situated before the fiber injection allowed {detector + electronics} IRF calibration.

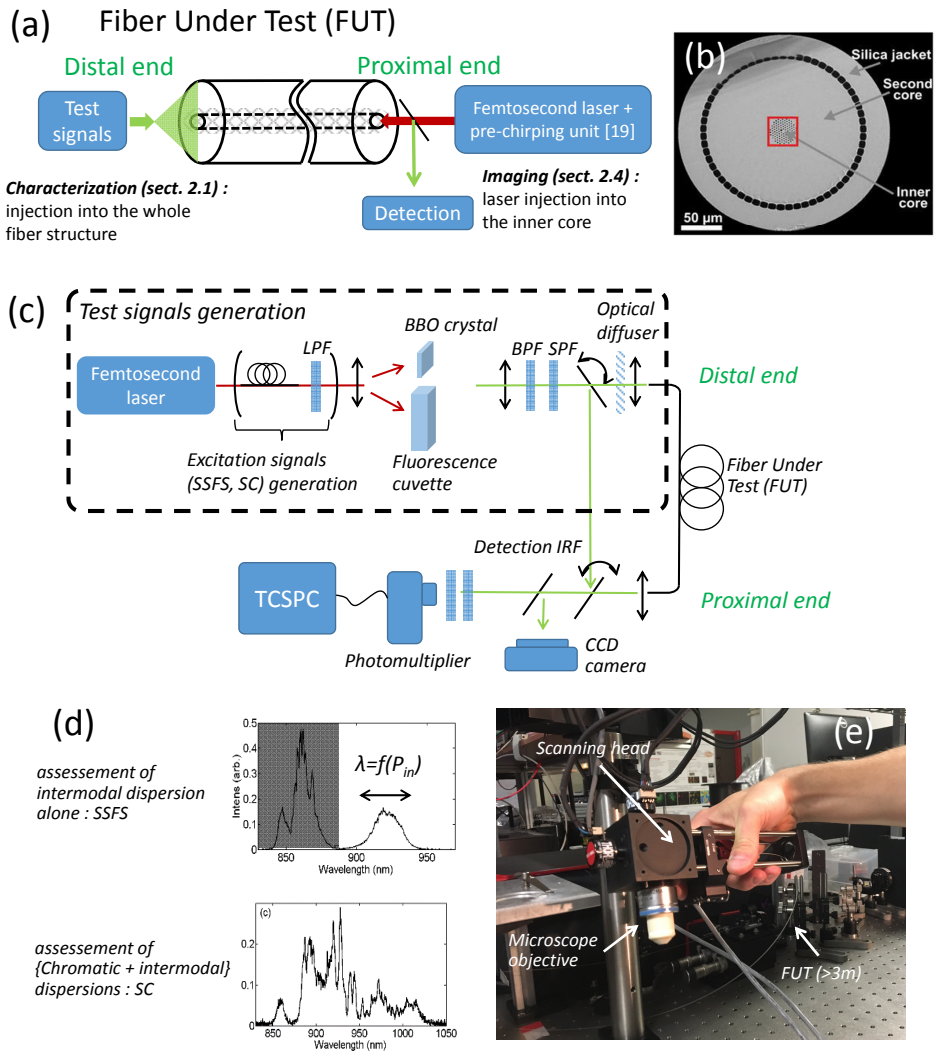

Fig. 1. Experimental setup. (a) Characterization vs imaging arrangement. (b) FUT microstructure (taken from [21]). (c) Experimental setup. SSFS: Soliton Self-Frequency Shift, SC: SuperContinuum, SHG: Second Harmonic Generation, LPF: long-pass filter, BPF: band-pass filter, SPF: short-pass filter, TCSPC: Time Correlated Single Photon Counting, IRF: Impulse Response Function, CCD: Coupled Charge Device, FUT: Fiber Under Test. (d) Typical excitation signals: SSFS ultrashort pulses (left) and spectrally broad supercontinuum (right). (e) Current scanning head for the imaging experiment.

Lifetime decays were composed of 10^4 to 10^5 counts to ensure a good signal to noise (SNR) ratio, adjusted using the excitation power, neutral densities before the detector and the TCSPC total counting time if required. Each free-space measurement (i.e. without fiber) was made directly before or after the corresponding fiber one to ensure similar measurement conditions. Fiber IRFs were fitted with Gaussian functions using OriginPro (OriginLab Corporation, Northampton, USA). Considering that the measured IRFs can be viewed as the convolution of the free-space and fiber IRFs, the FWHM duration of the fiber IRFs were

Biomedical Optics EXPRESS

obtained as $IRF_{fiber} = (IRF^2_{total} - IRF^2_{free\ space})^{1/2}$. Uncertainties were calculated, taking into account both fit uncertainties and statistical dispersion of measurements (Student's t-test $p<0.05$). Fluorescence lifetime histograms were deconvolved by their respective IRFs and fitted using the DecayFit software (www.Fluortools.com) to get the average lifetime. The uncertainty calculation was obtained as 4.3 times the standard deviation to get a 95% confidence interval in the lifetime values.

2.2 Fibers under test (FUTs)

The FUTs are double-clad PCFs similar to the one described in Ducourthial *et al.* [21]. They are composed of a 3.5-µm pure silica inner core (see Fig. 1(b)), separated from the 188-µm inner collection cladding (depicted as "second core", see Fig. 1(b)) by an air-filled pure silica microstructure. This pure silica fiber is devoid from auto-fluorescence generation contrary to doped silica fibers. The second core is separated from the outer silica jacket by an air clad. Their principal characteristics are summarized in the Table 1. Fiber A1 has been cut out from fiber A2.

Table 1. Tested fibers main properties

Fiber reference	A1	A2	B
Length (m)	4	8.15	6
Cladding NA	0.24	0.24	0.2

2.3 Phasor calculation and representation in imaging

We used the phasor representation [35,37], which provides a quicker and deeper insight than classic deconvolution or average lifetime representation while requiring less photons and computation time, as a non-fitting method. Phasor is a complex plane-like representation of our lifetime histograms, which coordinates are given by:

$$g(\omega) = \frac{\int_0^{+\infty} I(t)\cos(\omega t)dt}{\int_0^{+\infty} I(t)dt} \quad (1.1)$$

$$s(\omega) = \frac{\int_0^{+\infty} I(t)\sin(\omega t)dt}{\int_0^{+\infty} I(t)dt} \quad (1.2)$$

A monoexponential decay with a characteristic decay time τ will be located on a semi-circle going from {1,0} to {0,0} coordinates, the {1,0} point corresponding to $\tau = 0$ ns while the {0,0} one corresponding to $\tau = +\infty$. A multiexponential decay will be located on the center of mass of the polygon made from its monoexponential components. In the case of lifetime images, each pixel will give a point on the phasor with quick and agile binning capabilities. The lifetime histograms acquired had their maximum at t = 0s and they were corrected from a noise baseline before phasor calculations using Matlab (Mathworks) for the IRF and coumarin histograms and the MAPI software [37] for lifetime images on cells. In this case a 3x3 pixel binning was applied to the data and the lifetime image represents the mean lifetime value.

2.4 Fluorescence lifetime imaging

Imaging experiments were conducted on a fiber microscope similar to the one described in [38], where we used a 63x/1.15 NA water immersion objective (Zeiss) and the lifetime measurement modality instead of a spectrometer. A high NA lens (0.53, > 0.24 highest cladding one) was used to collimate the excitation pulses before the scanning head (and thus to inject the collected fluorescence into the fiber) and avoids measurement artefacts raising from modal selection (e.g. selective injection on the fiber lower modes). The scanning head

Biomedical Optics EXPRESS

could be freely operated in a user hand (see Fig. 1(e)). The configuration could deliver up to 110 mW @ 760 nm. Cell imaging was conducted using 20-25 mW of ≈50-100 fs pulses at the focal point. The laser was another Ti:Sa laser (MICRA, Coherent, Santa Clara, Ca, USA). Fluorescence photons were filtered by a 720 shortpass filter and a 460-80 nm bandpass one (Semrock) and were also detected using Hamamatsu H7422P-40 PMTs. Lifetime acquisition was done using a latency-free digitalizer (MCS6A, FAST Comtec GmbH, Berlin, Germany) with a 100ps resolution (50 ps using an interleaved treatment over 2 laser periods) and a 100 Mcps (Mega counts per second) peak count rate. This device allows for common dwell times (≈1-100 µs) and easy integration on fast imaging systems, the required amount of photons being acquired over several frames. Its IRF was measured, in free space, using the SHG signal of the MIRA laser focused on the BBO crystal, and on the fiber microscope using the SHG signal of collagen of a rat tail tendon sample. In this case the SHG signal was isolated from the collagen fluorescence using a 14-nm wide bandpass filter around 380 nm (FF01-380/14-25, Semrock). The intensity images were obtained by summing the photons of each histogram corresponding to each pixel. Lifetime images represents the mean lifetime for each pixel. FLIM data were collected until 200 to 300 photons in 10% of the pixels were collected. This signal level was obtained by the sum of 20 to 30 acquisitions. We choose an imaging configuration (200x200 pixels, 10 µs dwell time) to reach a > 1 fps (frames per second) possible imaging speed. The sample scanning was synchronized to the digitalizer acquisition, which imposed a transfer and treatment time after acquisition of a few seconds.

2.5 Cell cultures and treatments

HT29 colorectal cancer cells were maintained in McCoy's 5A medium (Gibco, Life Technologies) containing 1% antibiotics (penicillin-streptomycin) and 10% FBS at 37°C with a 5% CO_2. Just before imaging, culture medium was exchanged to Live Cell Imaging Solution (LCIS, Molecular Probes/Life Technologies) to avoid background fluorescence noise from the medium. Sodium cyanide (NaCN) in PBS was used to block the respiratory chain of the cells. It was diluted to 4 mM and cells were imaged immediately after NaCN addition.

3. Fiber characterization and suitability

3.1 Influence of the fiber dispersions on the IRF width

As NADH fluorescence is collected by the wide (188 µm in diameter, NA 0.2 to 0.24) fiber silica cladding, the material chromatic dispersion and the thousands of propagated modes will both result in modified arrival times of the fluorescence photons through the chromatic and intermodal dispersions. As a consequence the Impulse Response Function (or IRF) of the system is:

$$\begin{aligned} IRF_{total} &= IRF_{\det ection} * IRF_{fiber} \\ &= IRF_{\det ection} * (IRF_{chromatic} * IRF_{\text{int}er\,\text{mod}al}) \end{aligned} \quad (2)$$

with $IRF_{detection}$ being the IRF of the detector and the measurement electronics, $IRF_{chromatic}$ and $IRF_{intermodal}$ the IRF due to, respectively, the fiber chromatic and the intermodal dispersions, * the convolution product. Thus, we can expect that the full-width at half maximum (FWHM) of the fiber IRF fulfills:

$$\max(IRF_{chromatic}^{FWHM}, IRF_{\text{int}er\,\text{mod}al}^{FWHM}) \leq IRF_{fiber}^{FWHM} \leq IRF_{chromatic}^{FWHM} + IRF_{\text{int}er\,\text{mod}al}^{FWHM} \quad (3)$$

On the one hand, because of material chromatic dispersion, the silica refractive index evolves quickly in the NADH detection range (several tens of nm around 460 nm) and can lead to a strong contribution to the total IRF. Because of the width of the collection cladding, the contribution to the chromatic dispersion coming from the waveguide is supposed to be negligible in comparison with the one coming from the material (i.e. silica). The Fig. 2(a)

Biomedical Optics EXPRESS

shows the calculated pulse broadening as a function of the fiber length, taking into account only the fused silica chromatic dispersion [39] and considering typical detection bandwidths (50 and 80 nm) at a central wavelength of 450 nm [38]. In this configuration we find reasonable amounts of dispersion (< 400 ps) for relevant fiber lengths (5m) which is of the order of magnitude of our detector IRF FWHM (≈350 ps) and should not hamper lifetime measurements.

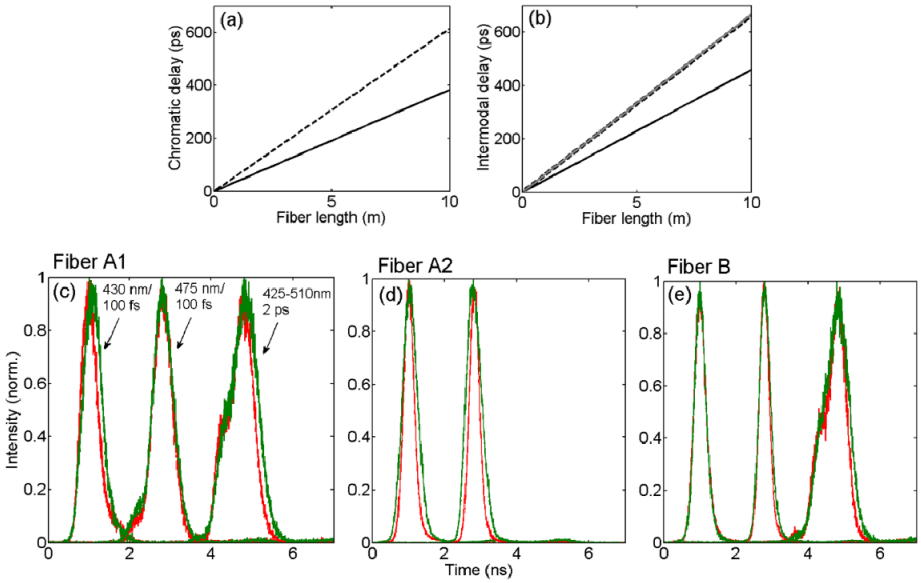

Fig. 2. Fiber dispersion influence estimation and characterization. (a) Calculated chromatic delay for a signal with a 50 (plain) and 80 (dashed) nm spectral bandwidth centered on 450 nm. (b) Calculated intermodal delay for a 400 nm carrier wavelength – 0.24 NA fiber (dashed black), 500 nm carrier wavelength – 0.24 NA fiber (plain grey) and a 450 nm carrier wavelength – 0.2 NA fiber (plain black). (c to e): Measured free-space (red) and fiber (green) IRFs. (c) Fiber A1 (0.24 NA, 4m). (d) Fiber A2 (0.24 NA, 8.15m). (e) Fiber B (0.2 NA, 6 m). On each plot, from left to right: 430 nm/100 fs pulses, 475 nm/100 fs pulses, 425-510 nm/2 ps supercontinuum. The fiber A2 was no longer available when using the supercontinuum.

On the other hand, the large number of fiber modes (≈6.10^3) within which fluorescence photons can be guided will impose an amount of intermodal dispersion that can be estimated using a rough geometrical optics approach:

$$\Delta t = \max\left(\frac{Ln_0(\lambda)}{c}\left(\frac{1}{\cos(\theta)}-1\right)\right), \qquad 0 \le \theta \le \theta_c(\lambda) \tag{4}$$

with L the fiber length, $n_0(\lambda)$ the pure silica refractive index [39], c the speed of light and $\theta_c(\lambda)$ the critical ray angle related to the inner cladding numerical aperture (NA). The Fig. 2(b) represents the temporal broadening induced by the intermodal dispersion as a function of the fiber length for the 2 kinds of fiber used. This broadening is also reasonable (< 400 ps) for relevant fiber lengths (5m) which is allowed by the moderate cladding NA (0.2 to 0.24). The 0.24 NA dispersion is of course higher than the 0.2 one so a compromise between collection efficiency and the intermodal dispersion should be sought. The carrier wavelength variation has only a limited influence on this dispersion, which we verified by our measurements. The fiber inner core is separated from this collection cladding by an air-silica microstructure which may perturb and filter the higher order modes. So we speculate that these estimations may somewhat overestimate the real effect of intermodal dispersion. An important

Biomedical Optics EXPRESS

observation is that we can expect a fiber IRF FWHM of less than 1 ns for up to a relevant 5-m fiber length. A more precise evaluation is to consider that

$$IRF \approx \sqrt{IRF_{chromatic}^2 + IRF_{\text{int}er\,\text{mod}al}^2} \quad (5)$$

taking into account gaussian shapes.

These durations can be handled by common lifetime imaging systems, e.g. through IRF deconvolution or direct phasor representation, so our fibers should be compatible with lifetime measurements.

IRF measurements on the different FUT are shown in Fig. 2(c to e). Their FWHM is given in Table 2. First, we consider the impact of intermodal dispersion on 4-m of the fiber A1 (Fig. 2(c)). We can notice a ≈350 ps detector IRF FWHM (free-space measurement, red plot) which is the expected order of magnitude for our detector [40]. We also confirm the limited effect of the wavelength on the intermodal dispersion in the working interval (values not shown in the table). We find an intermodal duration close to the calculations. As mentioned earlier we explain the little discrepancy as the possible impact of the fiber microstructure which could act as a "mode-filter", and thus advantages, e.g., the faster modes over the slower ones.

Using the supercontinuum, through which we can measure the impact of both dispersions, we find just a slight increase of the duration. As the Eq. (5) shows, this moderate increase is attributed to the convoluted nature of combination of the chromatic and intermodal dispersions. The supercontinuum non-flatness could favor some wavelengths and lower somewhat the effect of the chromatic dispersion, but we believe it to be wide enough to induce, still, a clear effect. In this case the slight detector IRF broadening had no consequence on the measurements as we can still notice an IRF broadening due to the presence of the FUT. Intermodal dispersion measurements made on the fiber A2 (Fig. 3(b)) lead to longer IRFs, but again shorter than expected, for which we cannot exclude manufacturing imperfections. This fiber length was no longer available when using the SC for measurements so the impact of chromatic dispersion could not be quantified. Finally, measurements were made on the fiber B which led, this time, to a lower value using the supercontinuum, which is surprising. Further investigation is required on this fiber, like the influence of the modal population and spectral transmission, to explain this behavior.

Table 2. Fibers' characterization metrics calculated dispersions compared to the deconvolved IRFs (rows 1 and 2), comparison between free-space and fiber coumarin 515 average lifetime (row 3).

Fiber	A1	A2	B
Intermodal dispersion IRF duration @ 430 nm - calc. / mes. (ps)	266 / 210 ± 27	546 / 294 ± 9	276 / 280 ± 26
Total fiber dispersion IRF (50 nm width) **Calc/Eq. (3) @ 430 nm** **Calc.Eq. (5)** **mes. (ps)**	266≤IRF≤510 312 /275 ± 35	550≤IRF≤1100 636 -	276≤IRF≤650 359 258 ± 42
Coumarin lifetime, deconvolution by the system IRF (ns) **Free space/fiber**	1.88 ± 0.04 / 1.81 ± 0.26	1.99 ± 0.04 / 1.91 ± 0.04	1.99 ± 0.04/ 1.86 ± 0.08

These measurements show that the fiber IRF, that is similar to the one from the detector, should not prevent fluorescence lifetime measurements. Especially the whole system IRF (fiber and measurement system) lies below 600 ps even for a long (8m) fiber which is perfectly suited to a clinical use. Fiber A (A1 or A2) is particularly suitable to endoscopic FLIM as it combines good collection efficiency to short IRFs. Such IRFs may not have to be deconvoluted, reducing the computation time and improving the overall imaging speed. As a perspective the collection NA could be even more increased to improve the detection efficiency and so the imaging speed, while being no detrimental to a precise measurement.

Biomedical Optics EXPRESS

3.2 IRF stability to fiber movements

The air clad around the fiber second core is related to a strong index difference which can tend to neglect mode leaking induced during fiber bending. Bending-induced mode coupling is a more subtle phenomenon which could induce a variability in the IRF and which influence is not easy to foresee. Hence one has to make sure that IRF variability, especially its peak variability, is not noticeable in the case of subtle NADH lifetime variation measurements.

We addressed this question by measuring the IRF center of mass variability for fibers A1, B (the fiber A2 was not available at the time of the measurements) which were subject to fiber movements typical of an imaging session (hand-induced random centimeters movements in the three directions, at a varying frequency of 1 to a few Hz), with curvature radii variations from several meters towards about 10 cm. We considered the difference between the maximum and minimum value of the center of mass, as a worst case variability parameter. We made 3 runs of 10 measurements for each condition. We used 100 fs /430 nm signals, populating all the possible modes thanks to a high NA injection objective complemented by a diffuser. In the case of fixed fibers, variabilities were below 70 ps which is comparable to the detection electronics ones. These measurements are shown in the Table 3.

Table 3. Influence of the fiber movements and curvature radius on the intermodal dispersion. The value represents the maximum difference between the different centers of mass (in picoseconds).

Fiber	Detection IRF	No movements	Movements
A1	12	19	18
B	28	52	49

We found differences of less than ≈50 ps again in all cases. This result confirms the fairly good stability of the modal population, even with fiber movement, for moderate bendings, as the air crown around the second core ensures a strong guiding. The pivotal point is that these variabilities are lower than typical variations of the NADH long lifetime component between sane and cancerous cell states (see [6], e.g.). Plus, the limited number of photons (typically < 1000/pixel [5]), required for fast image acquisition, will introduce even higher variabilities [37] so the modal population variability will not constitute the ultimate limitation of our system.

3.3 Validation using a reference dye

The suitability of our fibers was confirmed by comparing free-space and fiber measurements of the fluorescence lifetime of coumarin 515 in ethanol. The Fig. 3 shows typical lifetime histograms obtained, here, for fiber A2, i.e. for the less favorable conditions in terms of system IRF (the longest fiber with the highest NA). A good agreement between free space and fiber measurements is observed and is moreover consistent with the literature (1.9 ± 0.3 ns [41]). The Table 2 shows deconvoluted average lifetimes for all the FUTs. This deconvolution assumed mono-exponential decays which gave χ^2 systematically below 2, bi-exponential hypothesis did not show significant χ^2 reduction. Free-space and fiber mean lifetimes were similar (difference < 10%), except for the fiber B which also shows counterintuitive IRF measurements. We can notice a slight lifetime decrease, of no influence on the lifetime structure (similar mono-exponential fits and similar position on the phasor, see the Fig. 3(b)), which origin is under investigation. The difference in the average lifetimes between the different fiber lengths is also present in the free-space measurements and could originate from slight measurement calibration differences, not from the fibers themselves.

Biomedical Optics EXPRESS

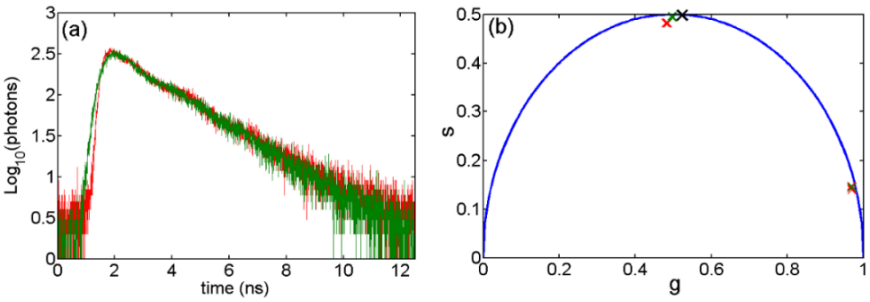

Fig. 3. Coumarin 515 fluorescence measurements through the fiber A2. Red = free-space. Green = fiber. (a) Typical TCSPC histograms. (b) Phasor representation. Coumarin fluorescence phasors are located near g = 0.5 and the IRFs near g = 0.95. Black cross: phasor corresponding to ref [41].

The phasor representation for fiber A2 (Fig. 3(b)) confirms the good agreement between free-space and fiber measurements and the literature [41] (black cross on Fig. 3(b)). We intentionally show raw lifetime histograms, without deconvolution, to highlight the suitability of this technique for quick representation. The slight lifetime decrease between free-space and fiber is visible. Especially, a major result is the suitability of our longest fiber (≈8m), which possesses in the same time a good collection NA (0.24). We confirm here our previous observation that an even better collection efficiency, using higher NA for reasonable fiber lengths (e.g. 5 to 6 m) is possible and would be beneficial to the imaging speed. Finally, the coumarin lifetime (≈2 ns), along with IRFs (≈400 ps) mimics quite well bound and free NADH lifetimes respectively. This shows that our fiber device could well discriminate different lifetime decays coming from different metabolic states, especially between marked states of very different lifetimes [8].

4. Validation by endogenous fluorescence lifetime imaging

The fast digitalizer used for lifetime imaging was calibrated and compared to the more widespread PicoQuant device used in section 3. We get a ≈430 ps IRF in free space (Fig. 4(a)) which is very similar to the PicoQuant one and adapted to lifetime imaging. We can see a slight difference in the temporal shape of its IRF compared to the PicoQuant device which results in a slightly different place on the phasor. This difference do not prevent lifetime measurements as we obtain a very good agreement, without deconvolution, between coumarin fluorescence phasors (see the Fig. 4(b)). Then the IRF of this digitalizer, integrated on the fiber microscope, was evaluated using the SHG signal generated on a rat tail tendon. We found a slight stretch to 560 ps as a result of the >3-m fiber dispersions (NA = 0.24), maybe due to the microscope detector which was different from the one used for fiber measurements and very partly to the collagen fluorescence [38,42], although being filtered out.

We made additional IRF variability measurements using the fibered microscope setup, where we induced the same fiber movements as described in sect. 3.2. We used the SHG signal coming from a rat tail tendon embedded into solid paraffin with diffusion miming a real tissue. We got variabilities of less than 100 ps, with a standard deviation of less than 50 ps, with no significant difference between a standing still and mobile fiber. Similar results were obtained with the fiber B. In that configuration the variability of the detection electronics could not be measured, but we can state that the fiber variability will be, at least, below these values.

Biomedical Optics EXPRESS

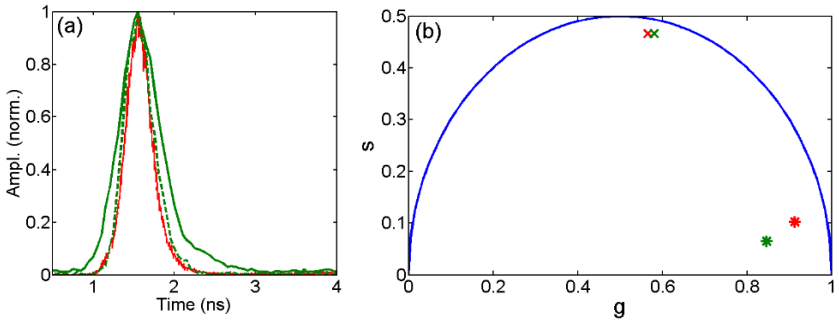

Fig. 4. Fast digitalizer suitability assessment using a 4-m/0.24 fiber. Red = PicoQuant reference device, green = Fast digitalizer. (a) IRF measurement using the Picoquant device (red), and the Fast digitalizer (dashed green) in free space, and the fast digitalizer in the fibered configuration (plain green). (b) Phasor of the IRFs (stars) and the raw coumarin histograms (crosses).

Finally, imaging was performed on label-free HT29 living cells to assess NADH lifetime imaging (Fig. 5). We can distinguish on the intensity image (Fig. 5(a1)) nuclei ghosts and a signal which mainly originates from the mitochondria [6]. The Fig. 5(a2) is the mean lifetime image of a 3x3 pixels binning followed by a 5 photon/bin threshold. High intensity regions shows a good overlap with lower lifetimes, but lower lifetimes do not exclusively overlap with them, which confirms that our lifetime imaging brings another point of view compared to intensity imaging. The phasor (Fig. 5(c)) was obtained by a 5x5 pixels binning and relates quite well to a combination of free and bound NADH [5]. Moreover a clear shift (from green to red) to a lower lifetime structure, in good agreement with the literature [10], can be seen after the addition of sodium cyanide (NaCN), which is known to block the cellular respiration and to lead to an accumulation of free NADH and thus to a lifetime downshift. This downshift can also be distinguished on the Fig. 5(b2), which shows the mean lifetime after NaCN addition. Finally, a ≈20% increase in the fluorescence signal was noticed which is consistent with the increase of the free NADH pool [43]. Importantly, these results were obtained using less than 150 photons/pixel, a 0.4-second frame acquisition time, and reproduced when fiber movements described in sect. 3.2 were induced (not shown), which confirms the potential of our configuration for a > 1 fps imaging speed and thus for real applications.

5. Discussion

In addition to this first proof of principle of nonlinear label-free FLIM through several meters of endoscopic fibers, many improvements and working directions can be considered. The current imaging frame rate is limited by the transfer and treatment delays from the digitalizer to the computer. These operations could be processed in parallel to intensity imaging to get a lifetime image in a few seconds or less along with video rate intensity imaging. If required the imaging part in contact with the tissues could be equipped with a suction system to avoid movement artefacts [44], allowing for medical or fundamental biology applications on patient or freely behaving specimens. Despite of our precautions noise was still present. An optimized noise reduction should reduce the number of acquisitions to less than 10 using this current setup and allow for an even higher frame rate (2.5 fps here). Specific developments using PCI cards like the PicoQuant TimeHARP 260 nano could also result in higher imaging photon flux and data transfer rate [45]. Concerning the optical part in itself, the collection cladding NA could be increased to collect more signal without being detrimental to lifetime precision (see sect. 2.1). Plus, the 760 nm excitation wavelength is chosen to lower the photodamage at the expense of the efficiency. Lowering it to 740 nm, along with overall optimization, should lead to quicker imaging. As a perspective, point-measurement has been

Biomedical Optics EXPRESS

made at the center of the truly miniaturized endoscopic configuration described in Ducourthial *et al* [26] and has led to similar IRF measurements. So we can hope for a very soon application of this technique to more integrated microendoscopes.

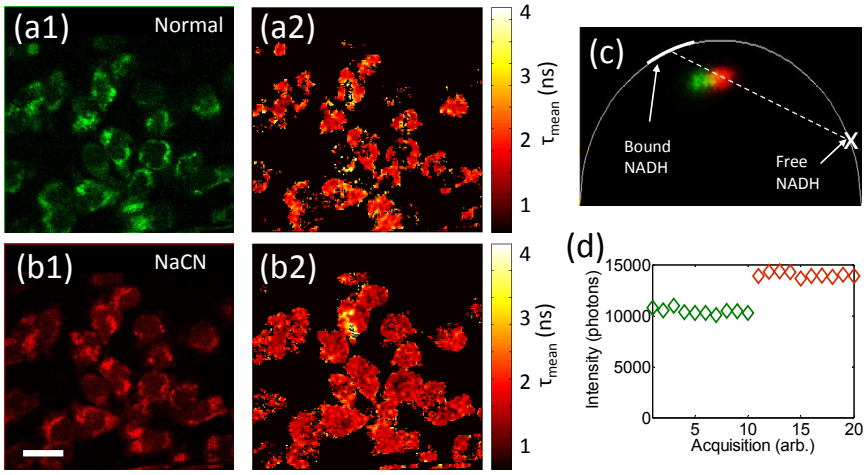

Fig. 5. HT29 cell lifetime imaging. (a1,a2) Before and (b1,b2) after addition of sodium cyanide (NaCN). (a1,b1) Intensity images, no binning. (a2,b2) Mean lifetime images, 3x3 pixels binning. (c) Phasor representation, 5x5 pixels binning. Free and bound NADH positions are taken from [5,6]. (d) Signal intensity evolution over the acquisitions. Scalebar = 20 µm. 200x200 px, 10 µs dwell time. Green = before and red = after NaCN addition.

6. Conclusion

We paved the way to nonlinear microendoscopic fluorescence lifetime imaging. The influence of intermodal and chromatic dispersion experienced by fluorescence photons collected by the endoscopic double-clad fiber were numerically evaluated and measured for 2 different meters-long special endoscopic fibers. These measurements lead to surprisingly low, but nevertheless partly explainable, dispersion values of 200 to 400 ps which can be accurately deconvoluted along with the detection IRF from lifetime measurements. Fluorescence lifetime measurements on coumarin confirmed the suitability of our fiber for lifetime nonlinear endoscopy and brought first evidence of possible NADH lifetime imaging possibility. First nonlinear NADH lifetime imaging finally validated our approach on an endomicroscopic configuration.

Funding

C.-H. Hage acknowledges the Région Limousin and the University of Limoges for financial support. Part of the materials were funded by the INSERM-Physicancer “FIMSTO” (2013) and “ENDOMETABOL” (2015) projects. C. Le Nézet acknowledges the Région Nord-pas-de-Calais (CPERs "intelligence ambiante", Axe 4: IRI and “Photonics for Society (P4S)”), and the project “G2progress” (ANR-13-BSV2-0016 for financial support

Acknowledgements

We warmly thank Dr. A. Tonello (Univ. of Limoges) for the loan of the PicoQuant device. We thank Pr. A. Desmoulières (GEIST CNRS/Limoges Univ. Laboratory, EA6309) for the gift of the HT29 cells and the rat tail tendon cuts in paraffin. We warmly thank A. Leray (LICB Laboratory, UMR 6303 CNRS/Univ. of Burgundy, Dijon, France) for his assistance on the MAPI software. We thank F. Braud (IEMN Laboratory, URM CNRS 8520, Villeneuve d’Ascq, France) and R. Habert (PhLAM Laboratory, UMR 8523 CNRS/Univ. of Lille) for

Biomedical Optics EXPRESS

their help on the fibers fabrication. We thank D. Pagnoux (CNRS/Univ. of Limoges) and R. Florentin (Univ. Limoges) for fruitful discussions on the modal population statistics.

Disclosures

The authors declare that there are no conflicts of interest related to this article.